Figure S1. Individual locations of the 107 modern and one ancient sample analyzed in the study.
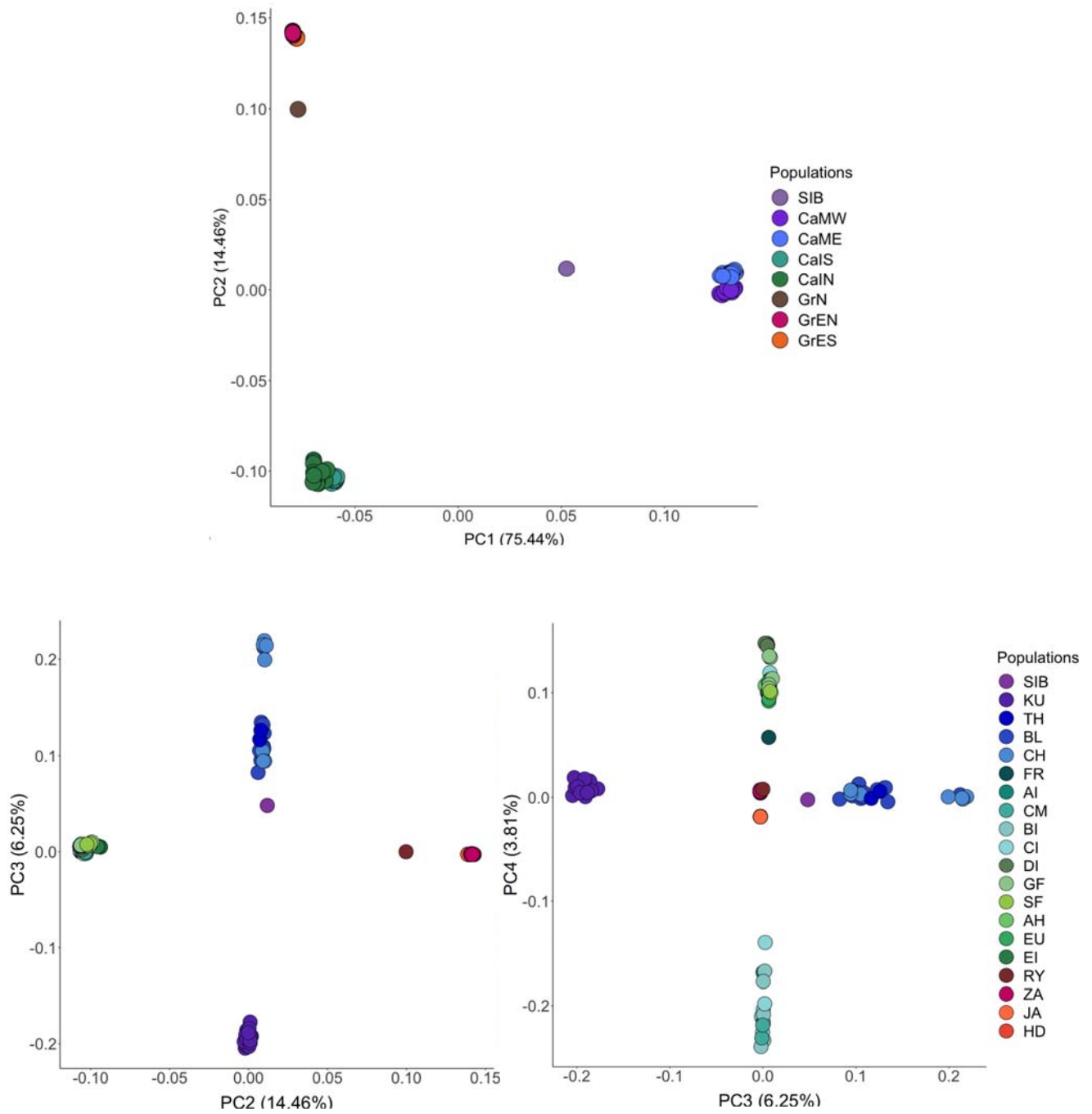
Figure S2. Principal components 1 to 4 of the PCA estimated in PCAngsd.
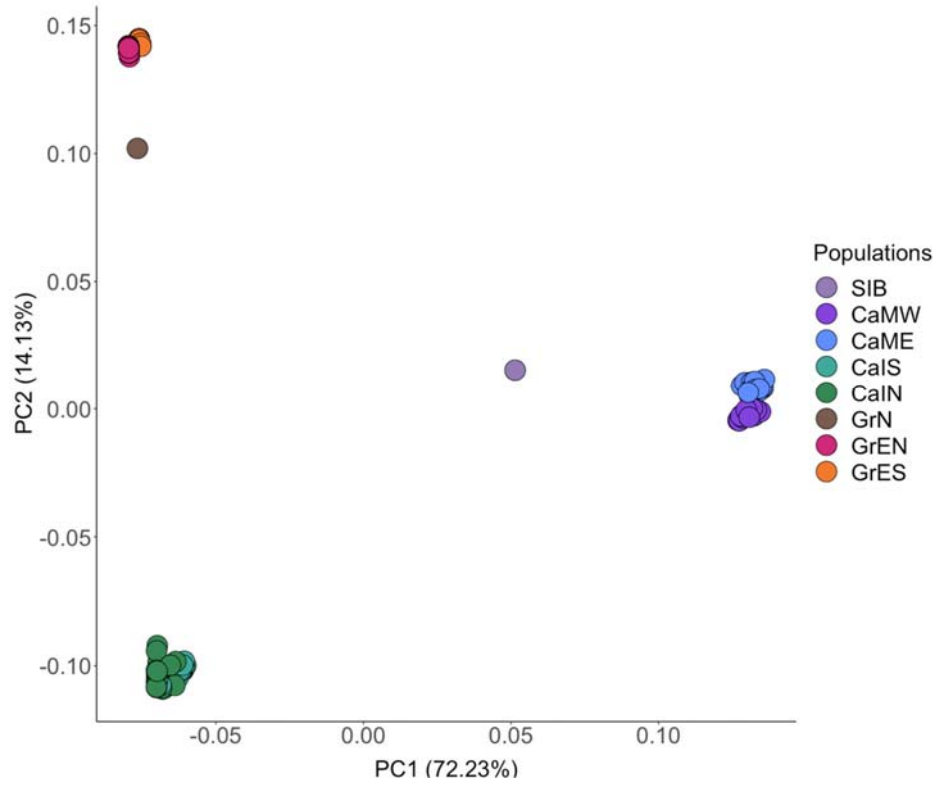
Figure S3. Principal components 1 and 2 of the PCA estimated in PCAngsd based on sheep-mapped data.
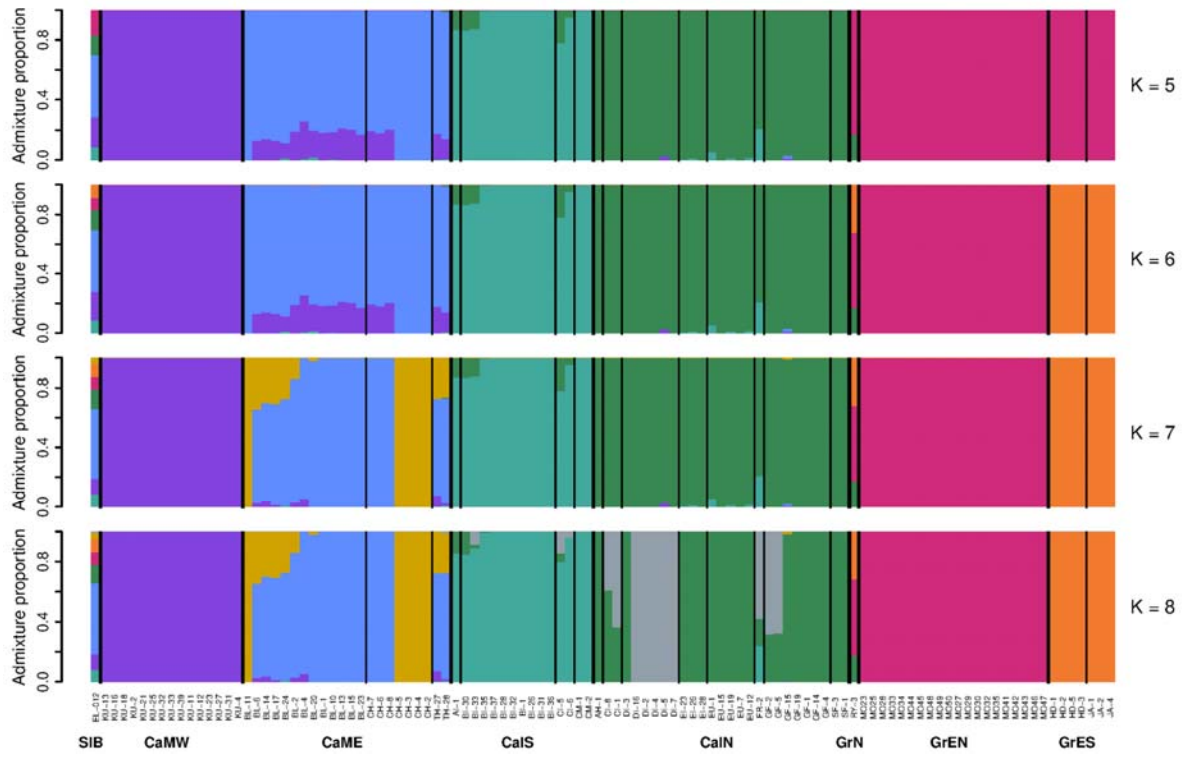
Figure S4. Admixture proportions inferred by NgsAdmix for each individual at K=5 to K=8 grouped by locations (black vertical lines) within a region (y-axis labels).
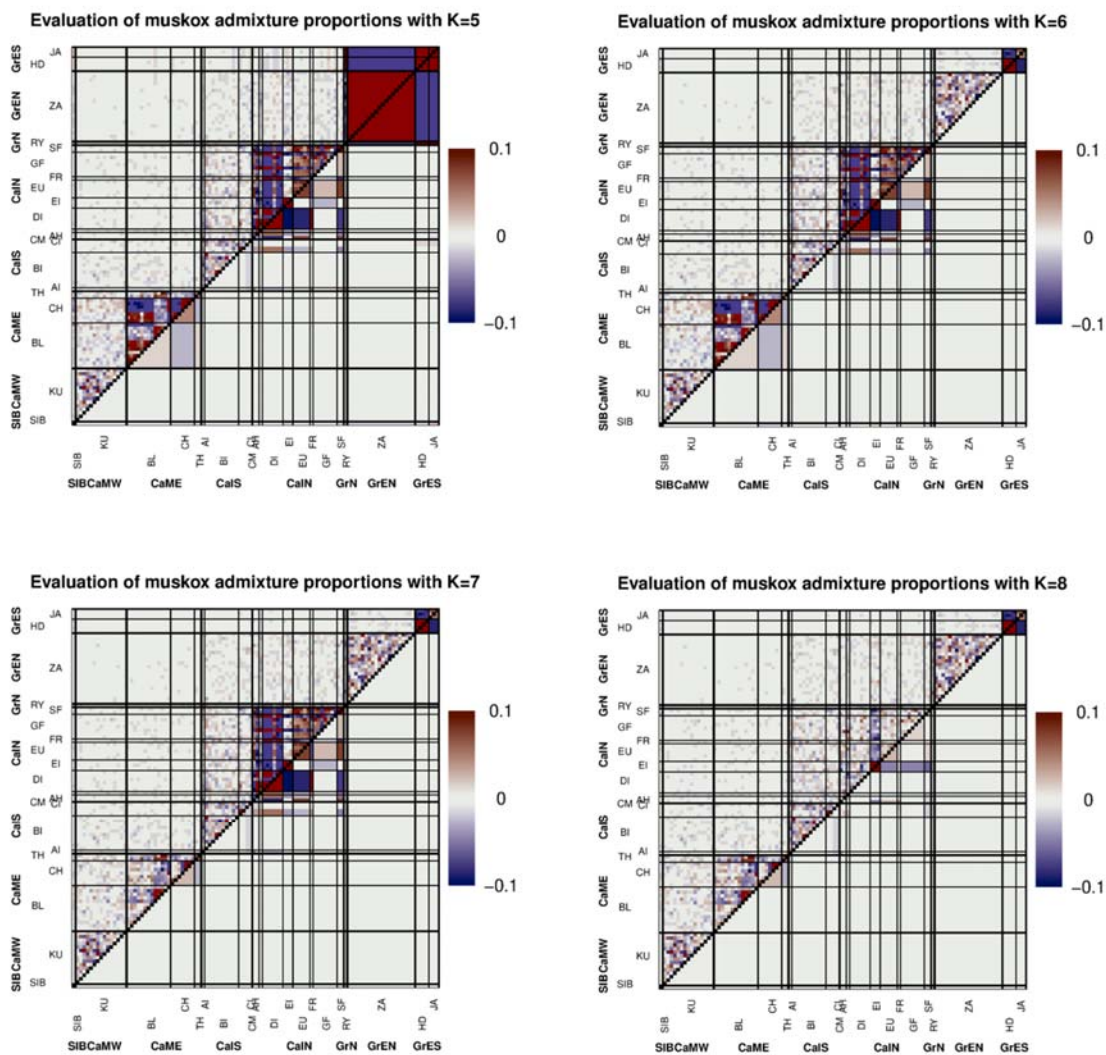
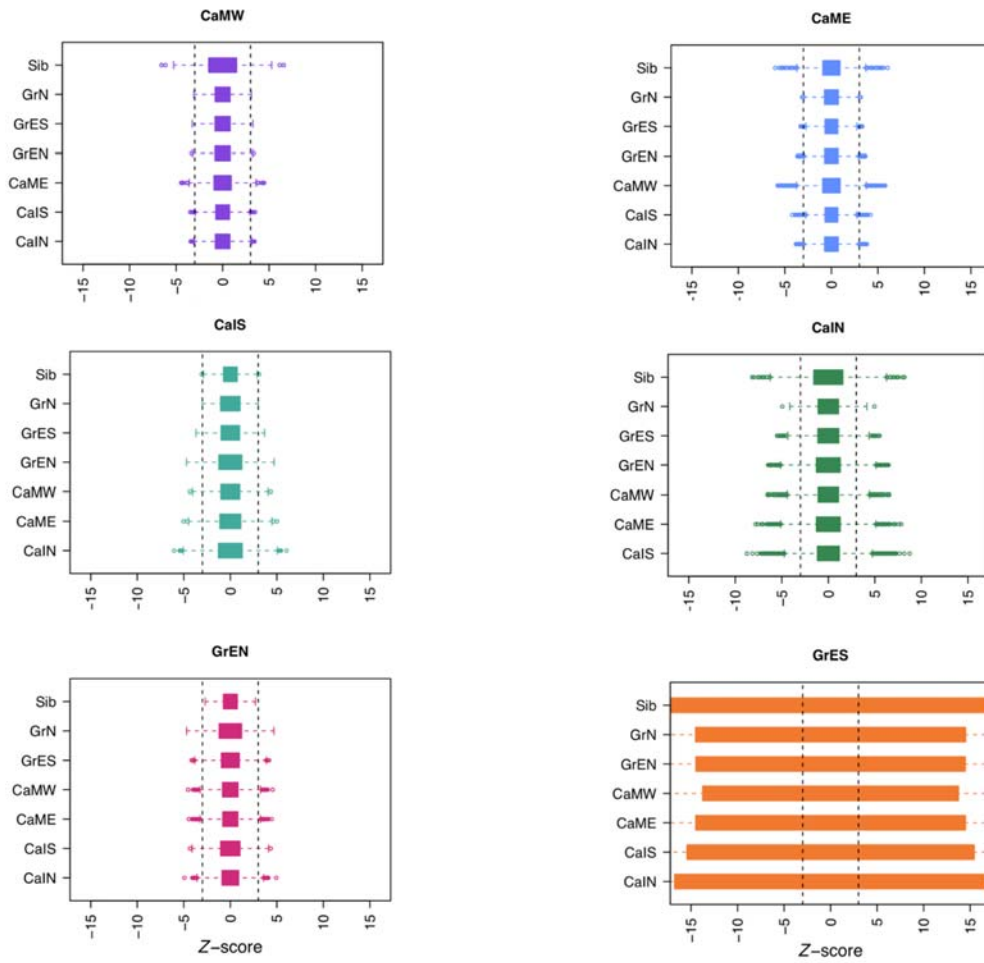**Figure S5.** Evaladmix for each individual at K=5 to K=8.

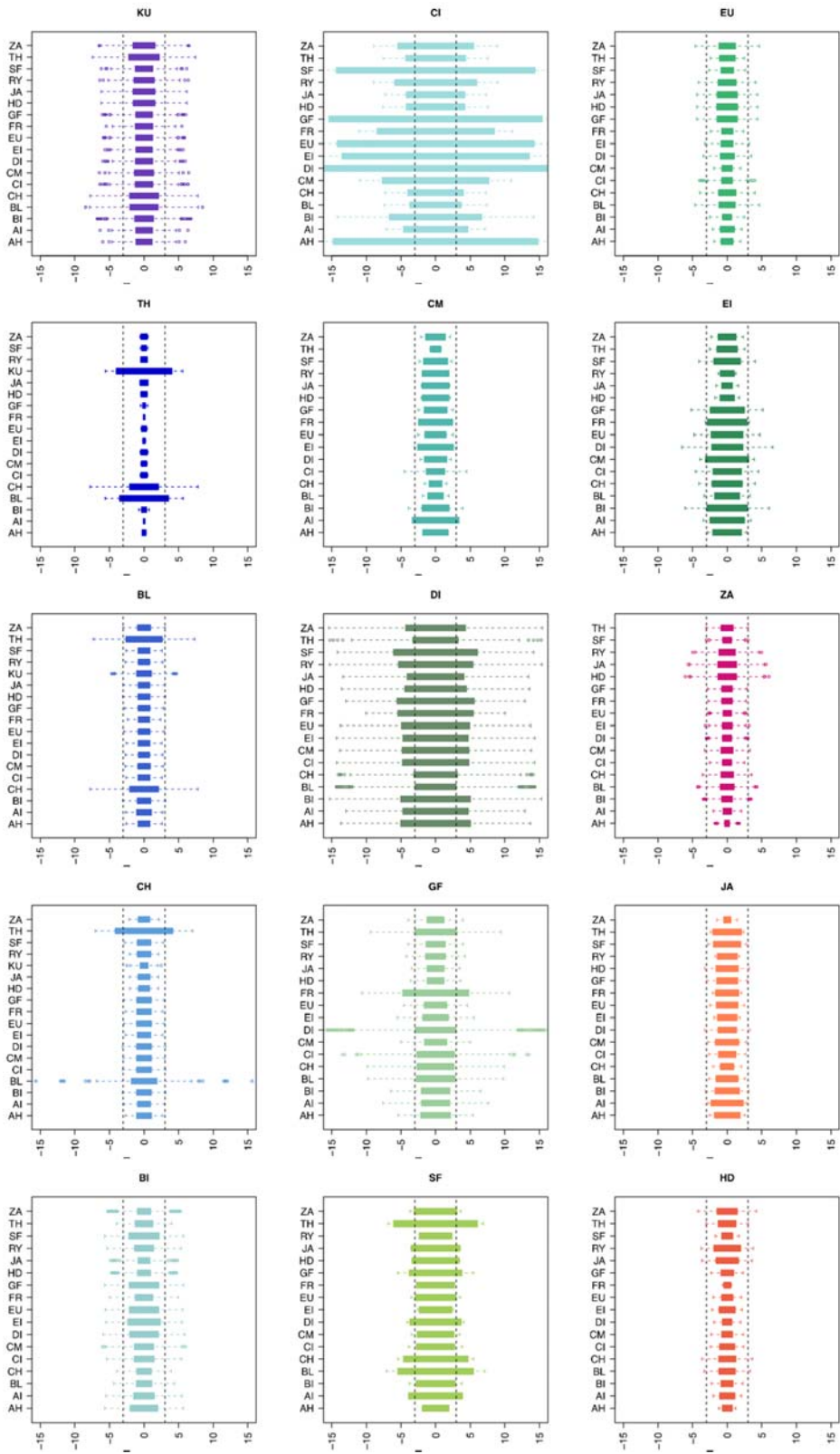**Figure S6.** Population homogeneity within regions.

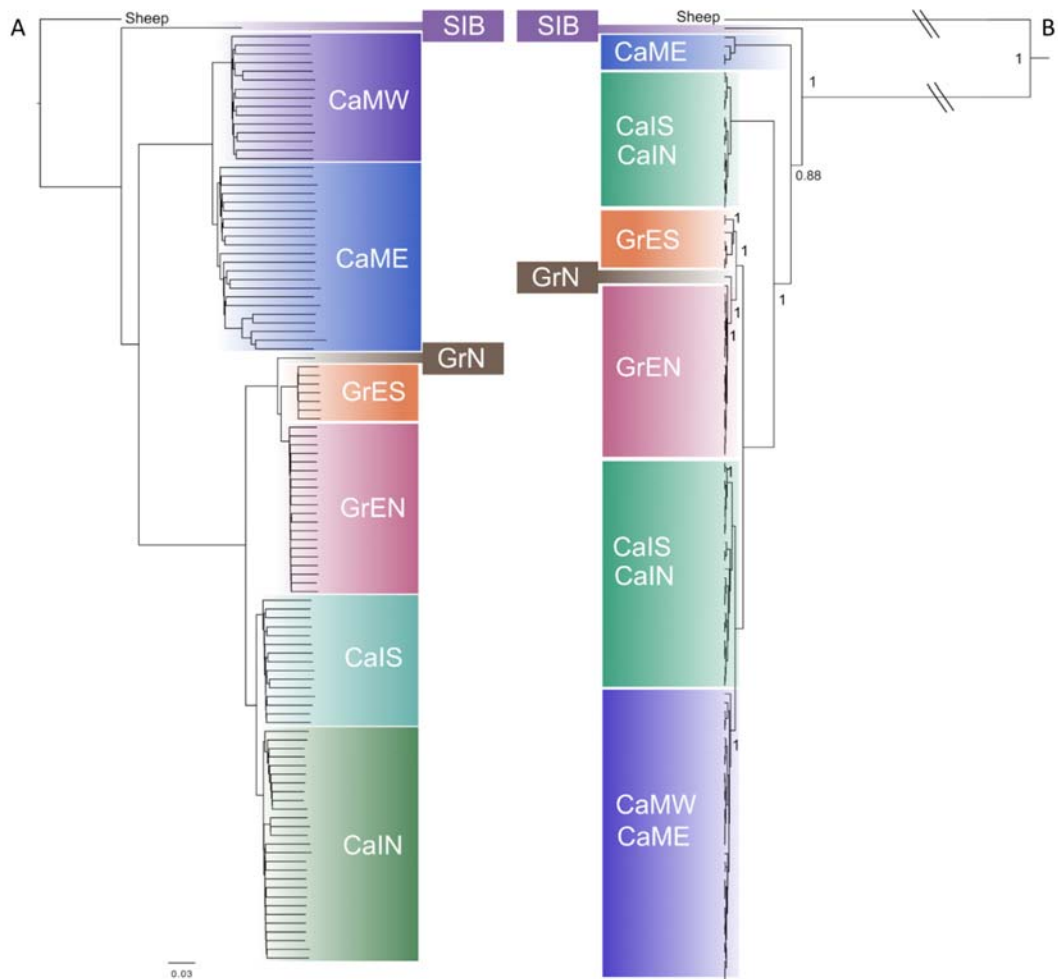**Figure S7.** Population homogeneity within locations.

Figure S8. Different genetic relationships estimated using nuclear and mitochondrial data. A) A neighbour-joining tree of genetic distances based on an IBS matrix estimated in ANGSD. B) A mitogenome phylogeny estimated in BEAST; node labels indicate posterior support >0.7 and dashed lines indicate where the branches were shortened for visualization purposes.
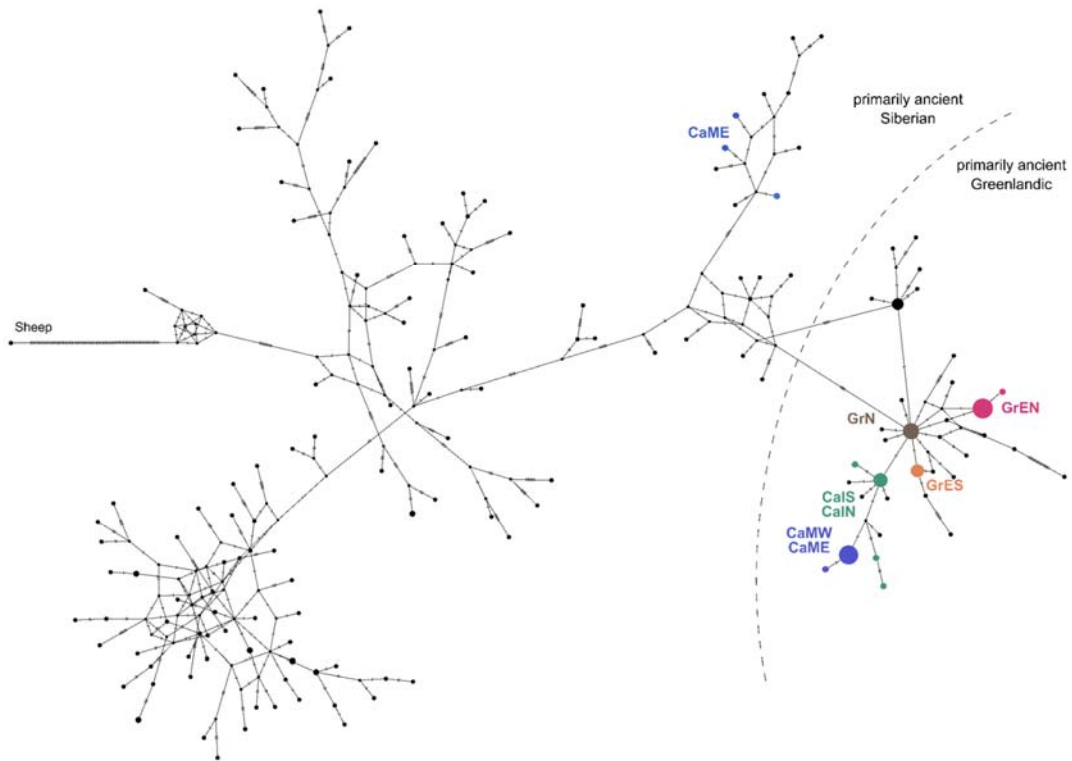
Figure S9. Median-joining network of all modern (this study) and ancient samples (this study and Campos et al. 2010).
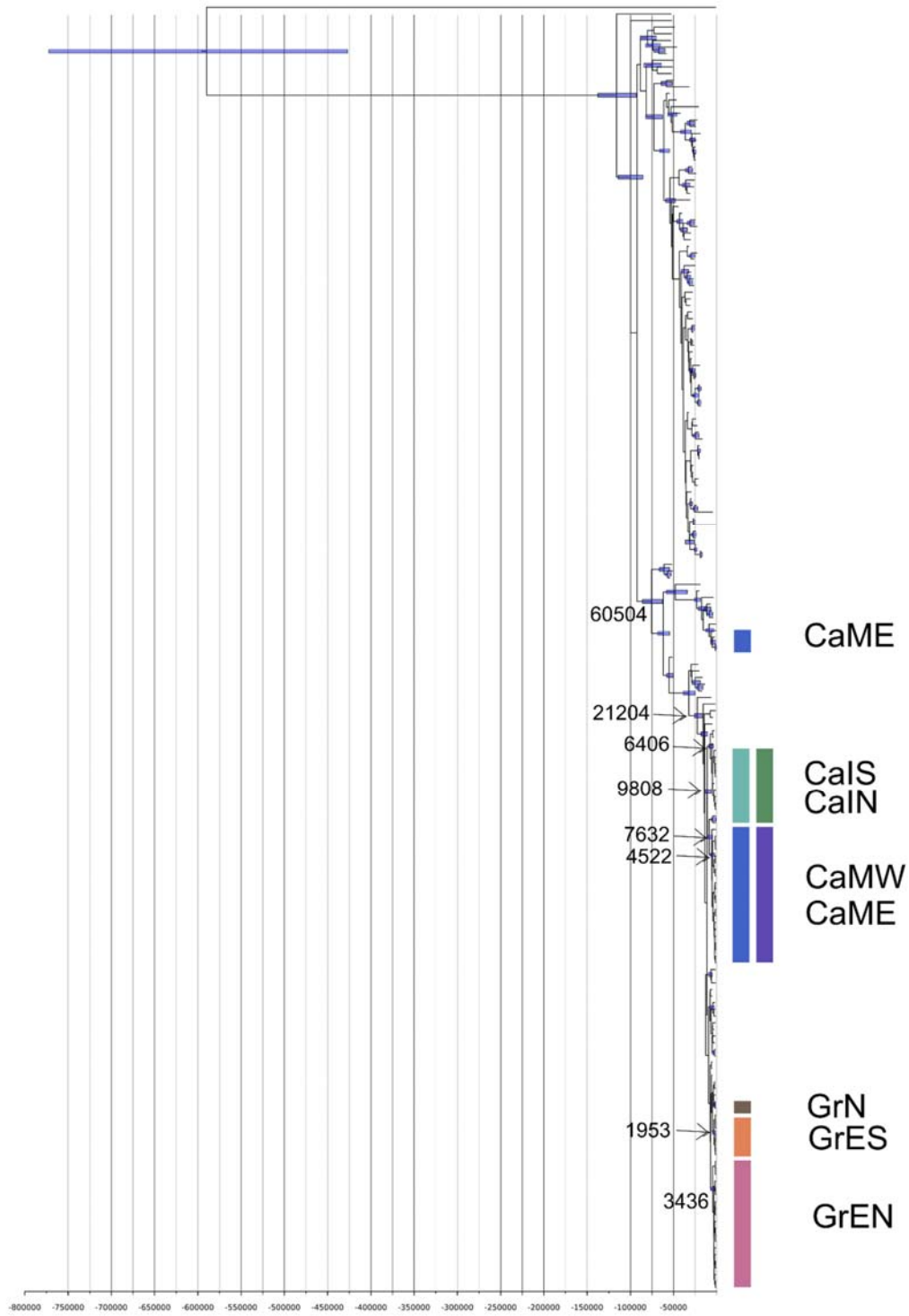
Figure S10. A Bayesian phylogeny estimated in BEAST based on 875 base pairs of the mitochondrial control region and a total of 194 samples, including the modern sequences generated in this study (highlighted) in the context of previously published ancient DNA sequences (Campos et al. 2010).
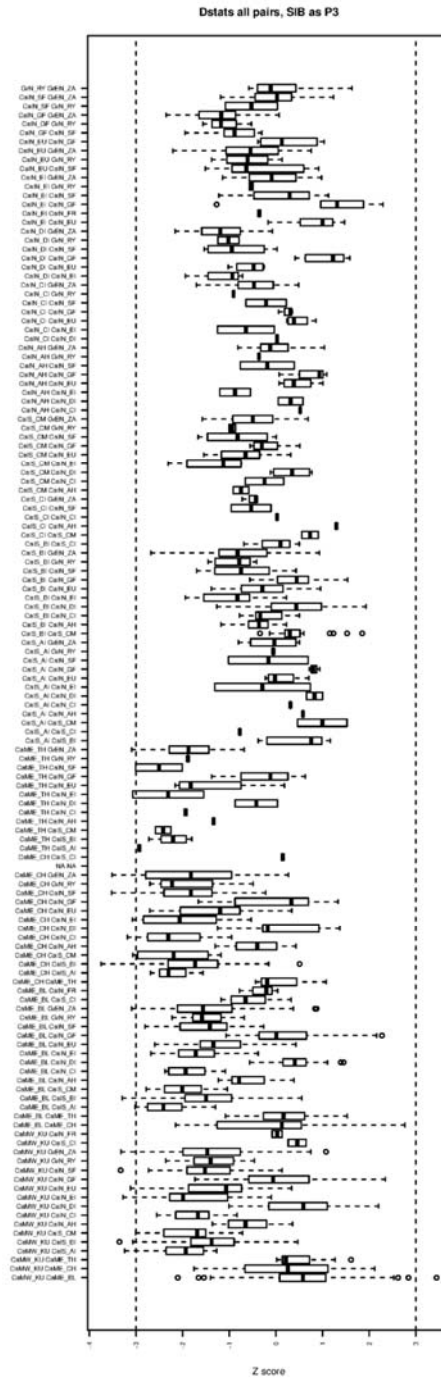
Figure S11. The same Bayesian phylogeny of control region sequences shown above, but here as a cladogram to aid visualizing the estimated posterior probabilities (shown as branch labels) and 95% highest posterior density of inferred node ages (shown as node labels). Previously published samples are labeled with the location of origin, calibrated radiocarbon age in calBP, and GenBank accession number.

Figure S12. D-statistics comparing all pairs of modern populations (as P1 and P2) to the ancient Siberian muskox (as P3), with the sheep as outgroup, based on genotype calls. We removed the HD and JA populations, which showed biased results because the low variation makes the estimate more sensitive to errors and the long runs of homozygosity make the Z score unreliable.
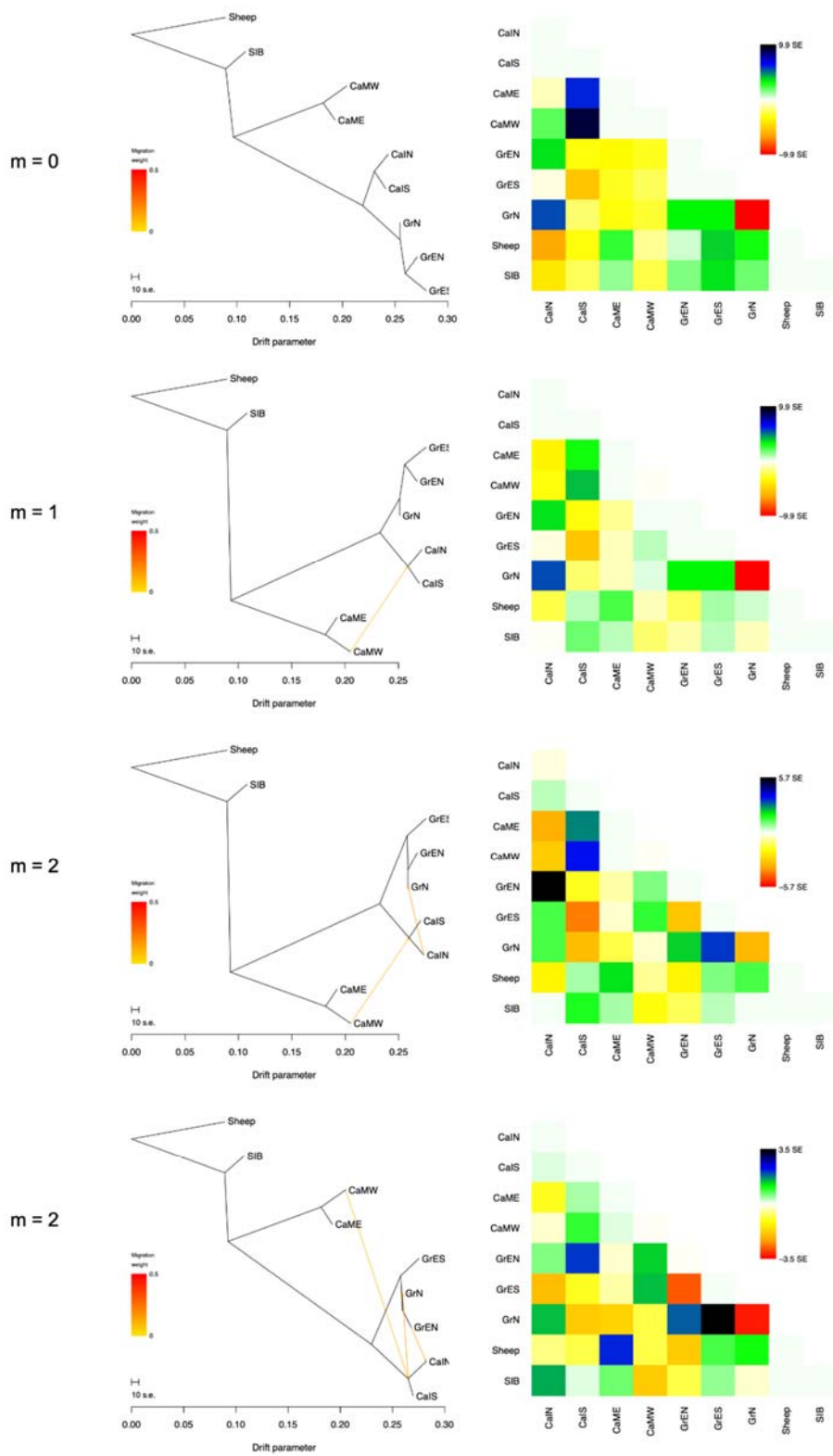
12

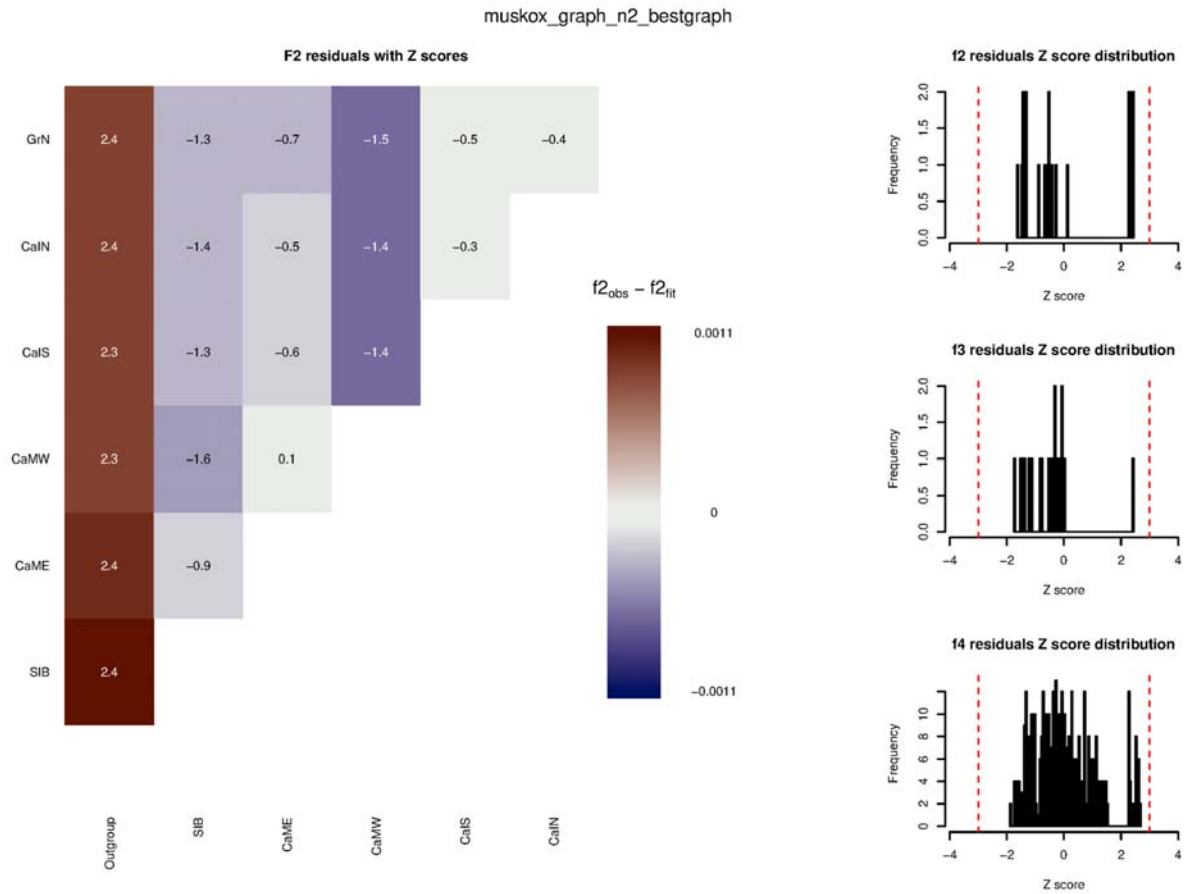**Figure S13.** Treemix with 0 to 2 migration edges.

13

Figure S14. Estimation of residual f-statistics from qpGraph showing that there are no significantly deviating residual f-statistics.
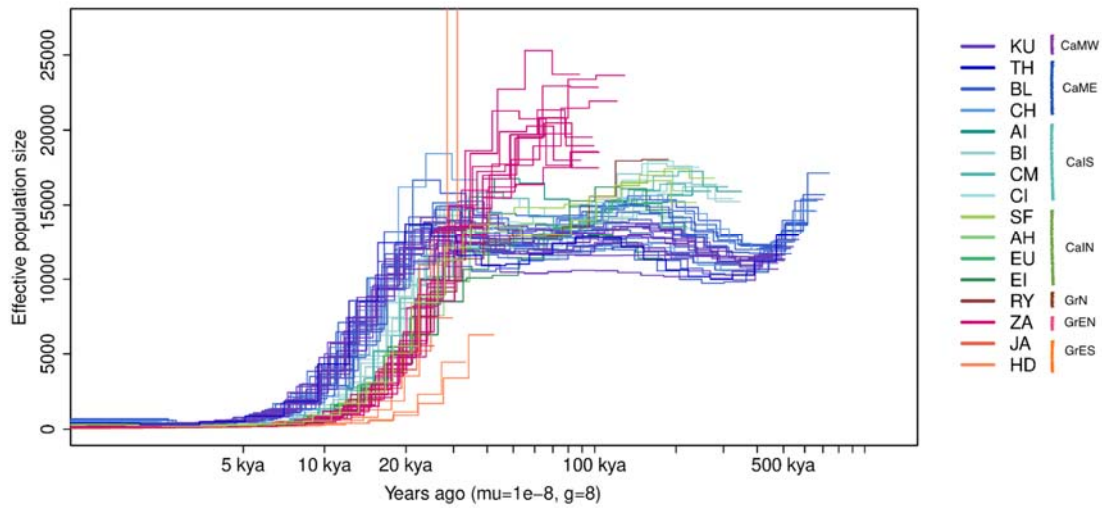
Figure S15. Reconstruction of effective population size through time using Pairwise Sequential Markovian Coalescent (PSMC), using the ancient Siberian muskox and the present-day Canadian and Greenlandic muskoxen.
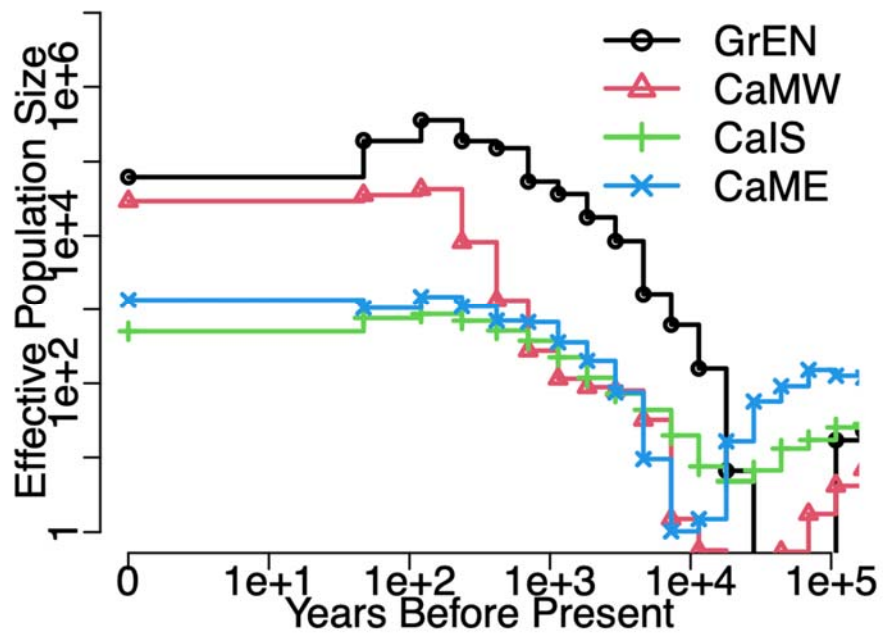

Figure S16. Approximate Bayesian estimation of the effective population sizes in the more recent past using PopSizeABC.
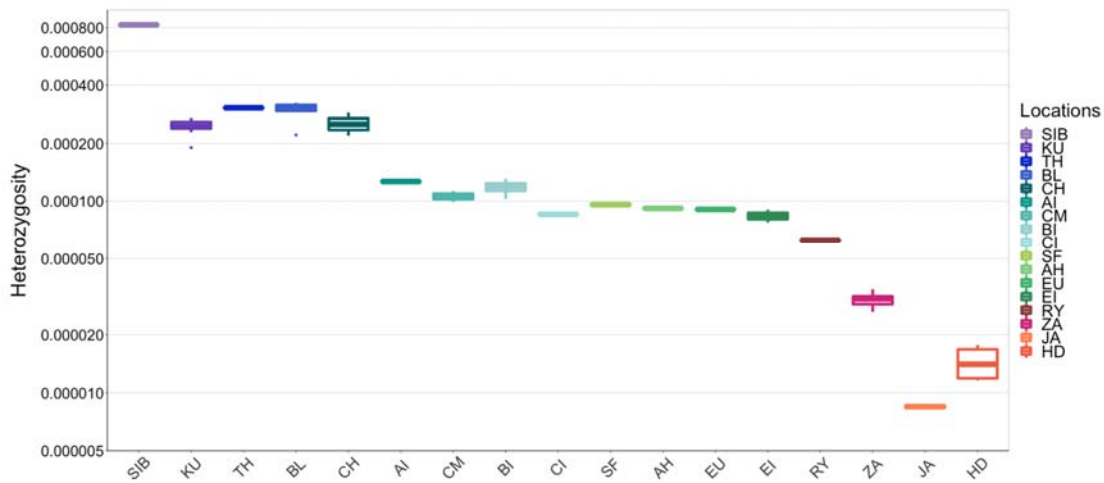
Figure S17. Genome-wide heterozygosity estimates based on genotype calls shown in Figure 4, but with y-axis in log10-scale for better visualization of the differences between low heterozygosity populations.
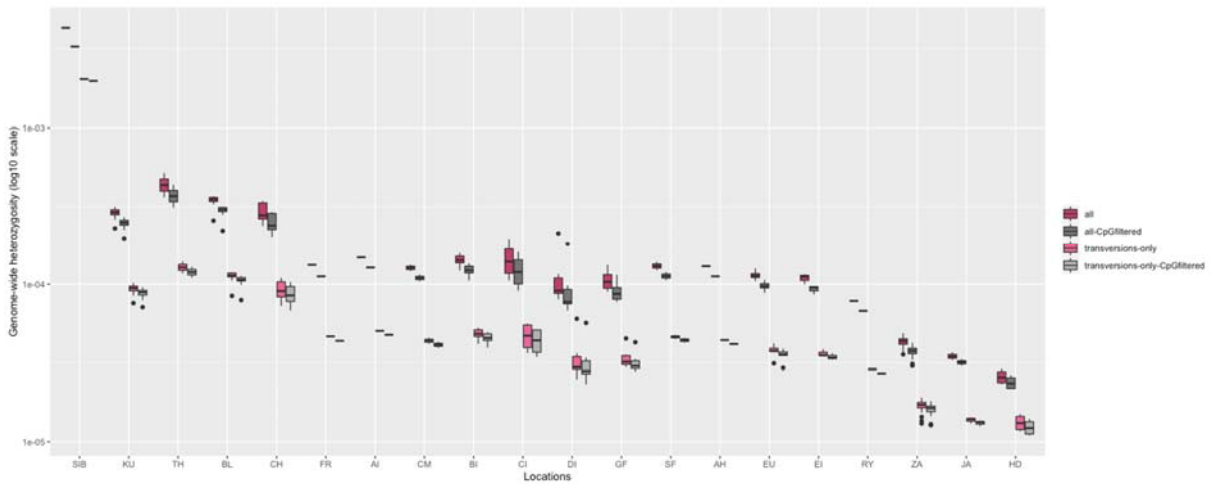

Figure S18. A comparison of the heterozygosity estimates from 1d SFS based on genotype likelihoods with (dark) and without (light) transitions, and including (pink) and excluding (grey) CpG sites which might potentially harbour elevated error rates, but the estimates show that the ancient sample does not deviate from the pattern observed in the modern data. The y-axis is in log10 scale.
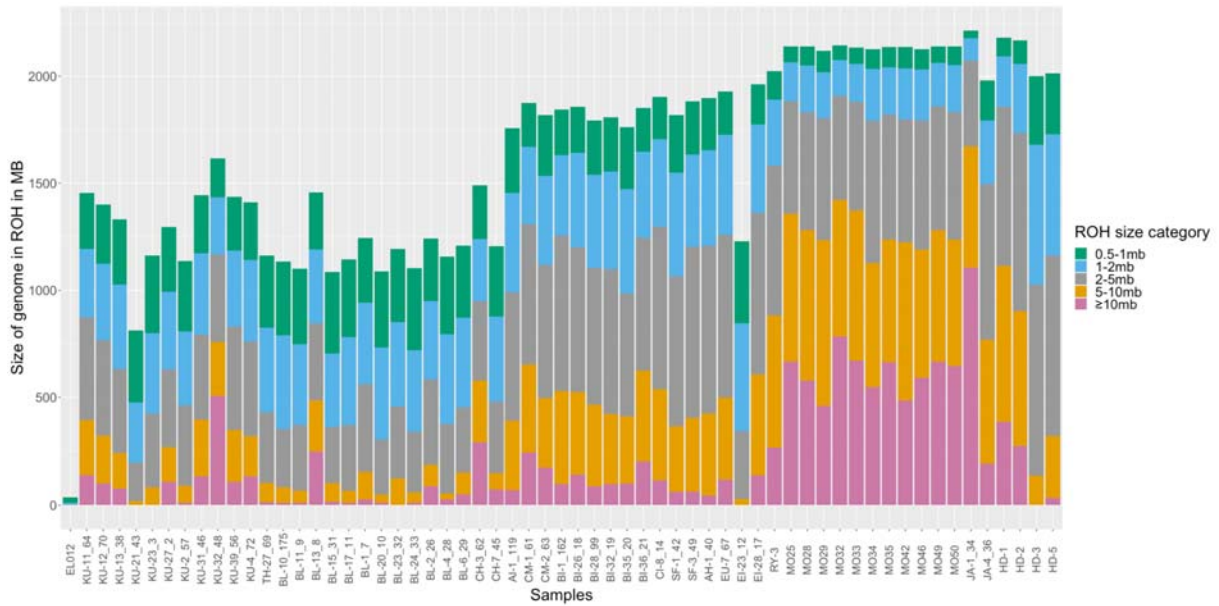
Figure S19. Size of ROH in MB estimated in PLINK for each individual shown distributed in the various size categories. For the calculation of inbreeding coefficients (F_{ROH}) only ROH of at least 1 MB were considered.

Figure S20. An example of validation of the ROH estimated in PLINK for 10 medium-sized scaffolds of two individuals, (a) representing individual KU-39 from the CaMW region with relatively high levels of heterozygosity and low ROH proportion, and (b) representing individual MO50 from the GrEN region with relatively low heterozygosity and high ROH proportion. The top black bar indicates ROH location estimated in the PLINK analysis. In the second bar, blue represents regions with only homozygous sites and red represents regions containing both heterozygous and homozygous sites. Grey shows the proportion of heterozygous SNP in the window, and purple indicates SNP density.
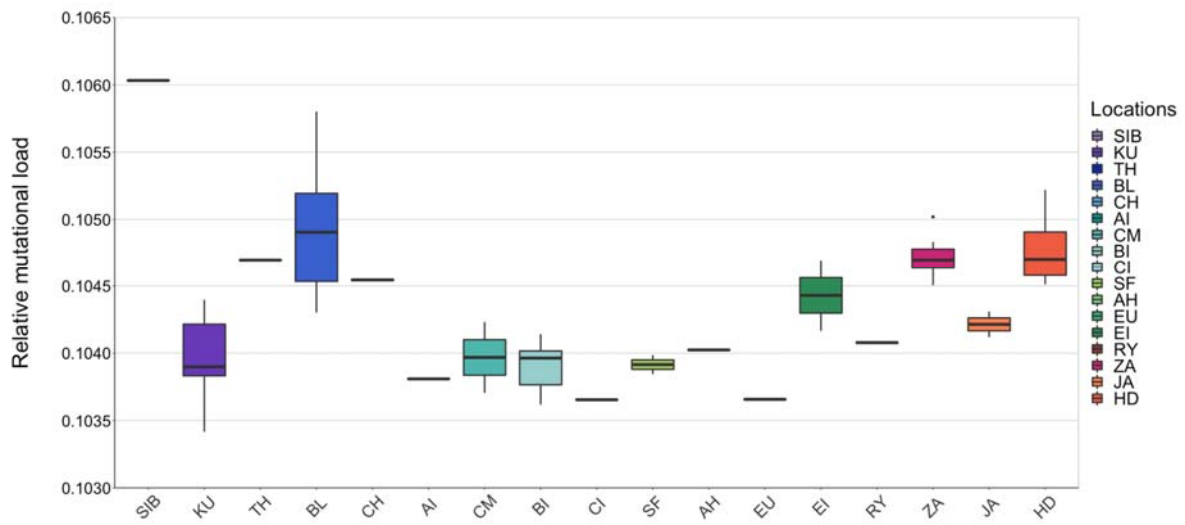
Figure S21. Relative mutational load estimated using GERP on the muskox-mapped dataset of 277,370 sites represented in all individuals.
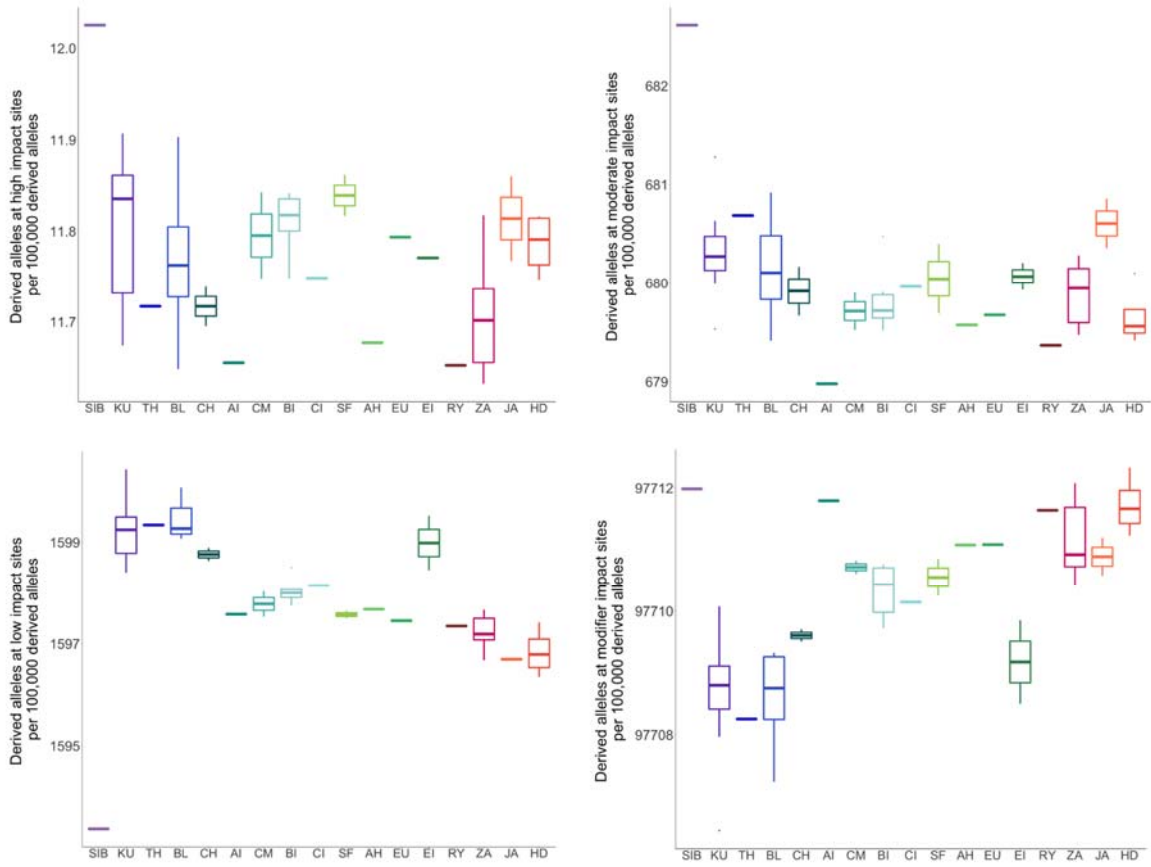
Figure S22. Total mutational load estimated in SNPeff using the sheep-mapped dataset of 2,309,442 sites present in all individuals, calculated as the proportion of derived alleles at sites belonging to an impact category per 100,000 derived alleles.
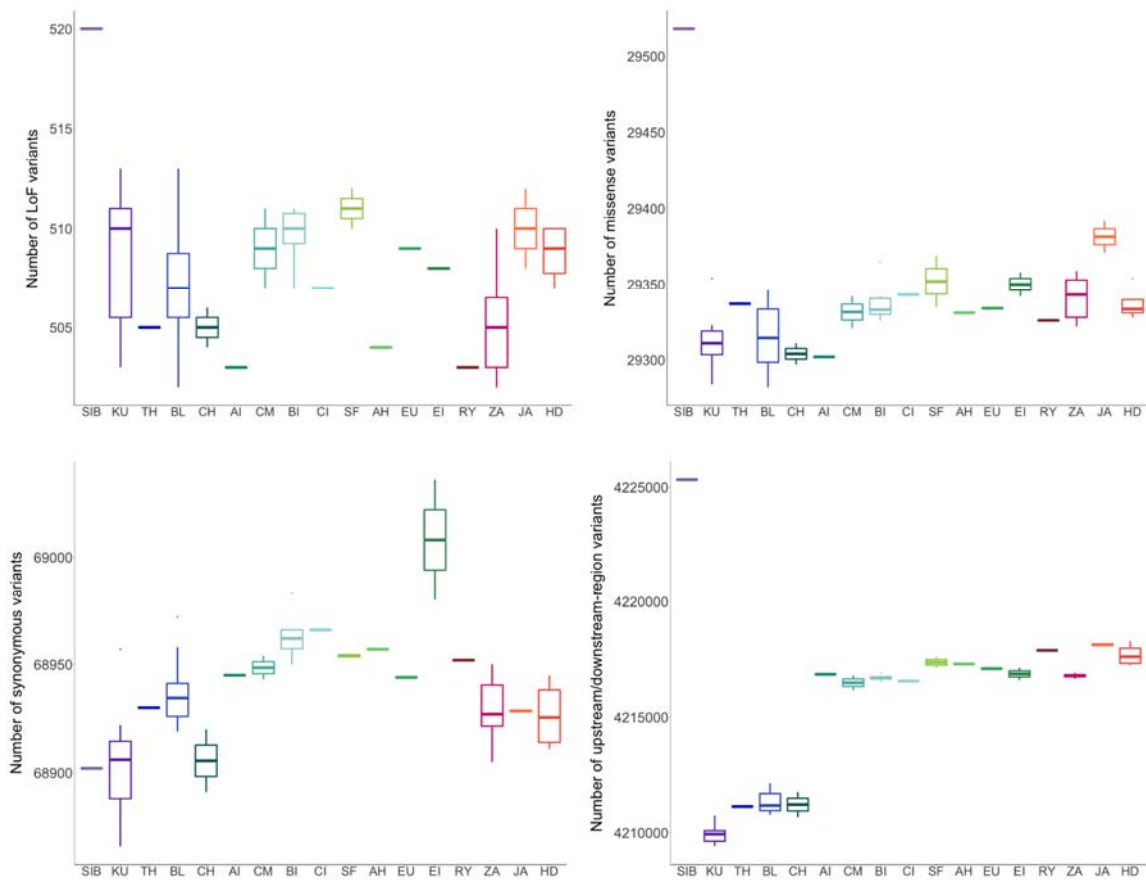
Figure S23. Number of variants per individual stratified by functional annotation. Variants were annotated by SNPeff using the sheep-mapped dataset of 2,309,442 sites without missing genotypes.
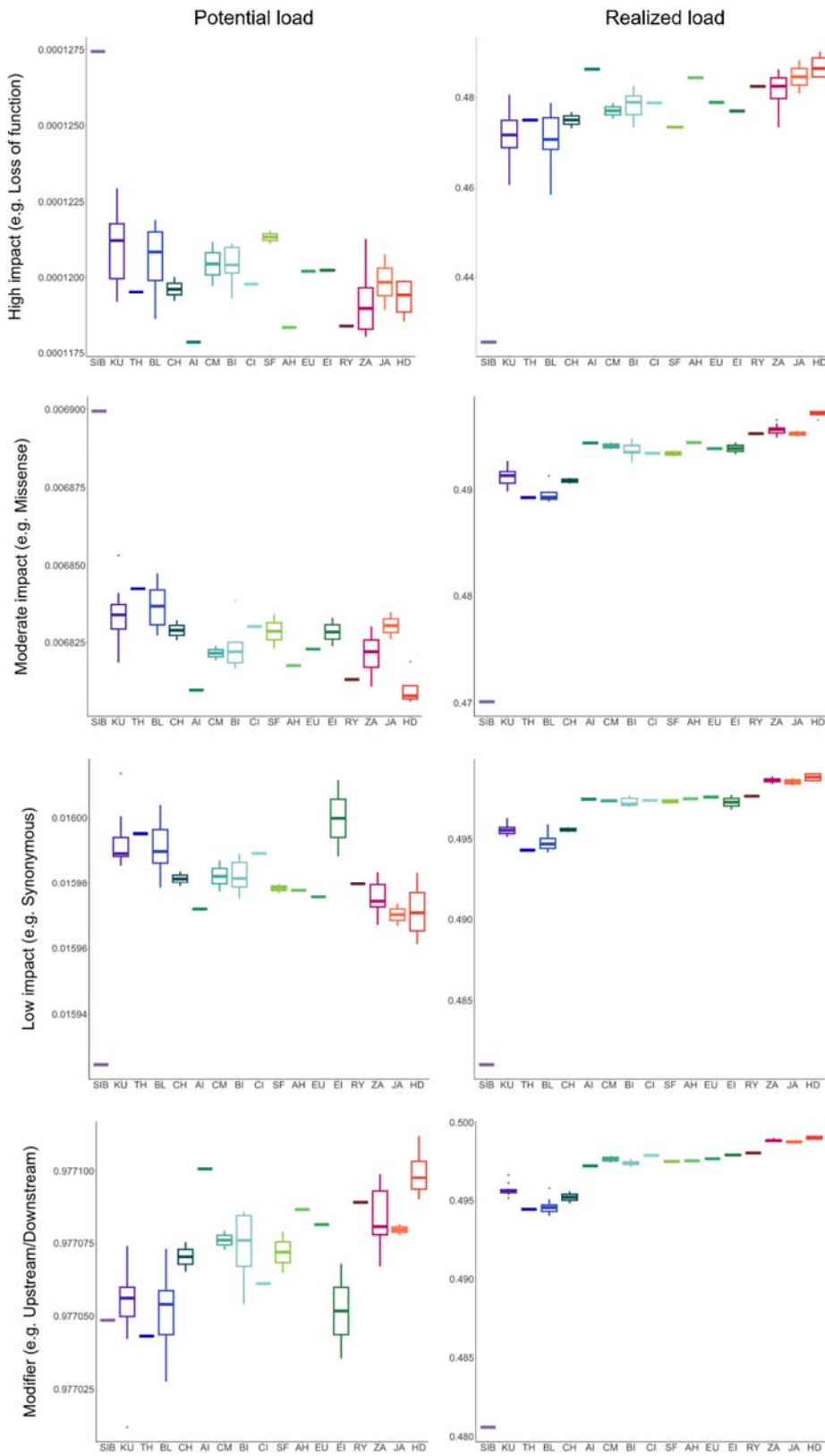
Figure S24. Potential and realised load estimated based on functional annotation by SNPeff using the sheep-mapped dataset of 2,309,442 sites without missing genotypes, calculated as a fraction of sites in an impact category (potential load) and as fraction of sites that are homozygous in an impact category (realised load).
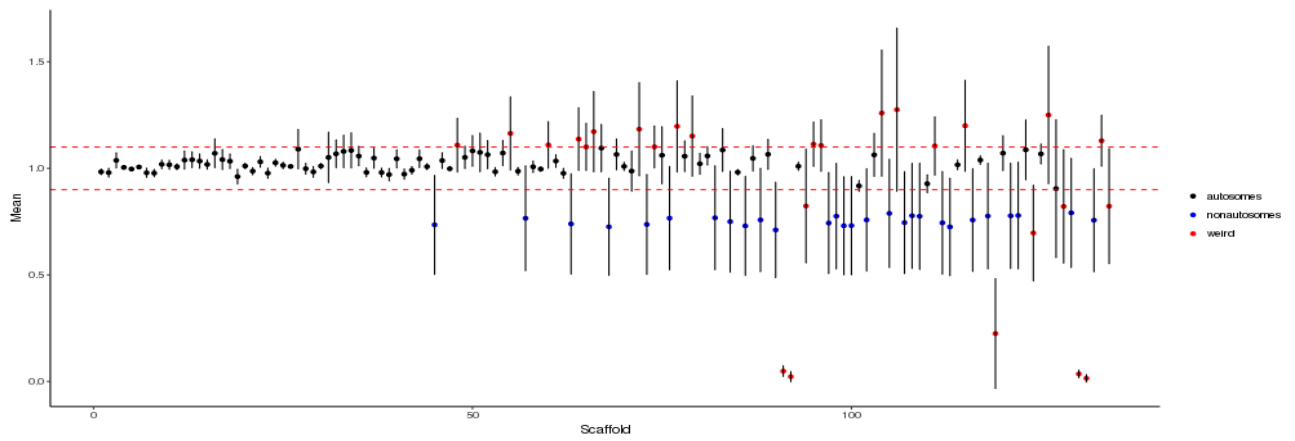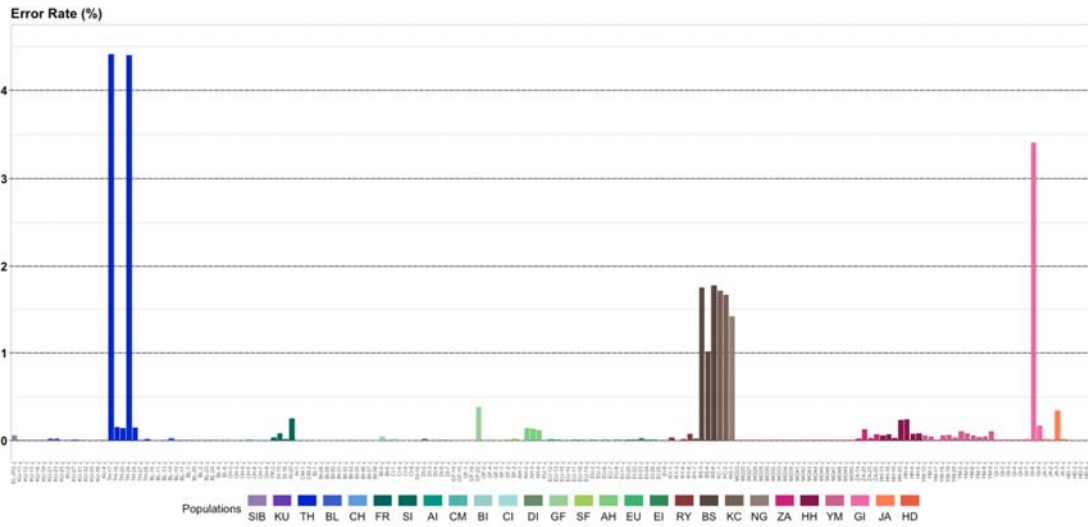
Figure S25. Determination of potential non-autosomal scaffolds in the muskox reference genome based on an analysis using the SATC method (Nursyifa et al. 2022). Scaffolds with suspicious patterns of depth distribution were removed from further analysis and only the 69 scaffolds within the dashed bounds were retained.
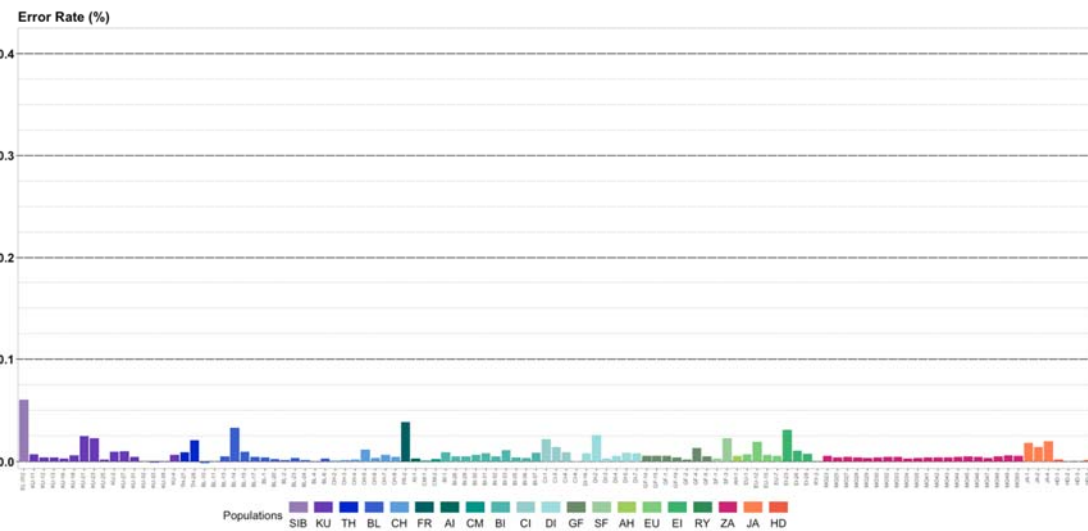
(a)

(b)

Figure S26. Relative error rates estimated using the 'perfect-sample' approach (Orlando et al. 2013) where an excess of derived alleles is calculated in comparison to a high-quality sample. (a) Including the Siberian genome and all 178 modern genomes; (b) Including only samples used for analyses. Notice that the error rate is estimated before applying the filter that removes CpG sites.
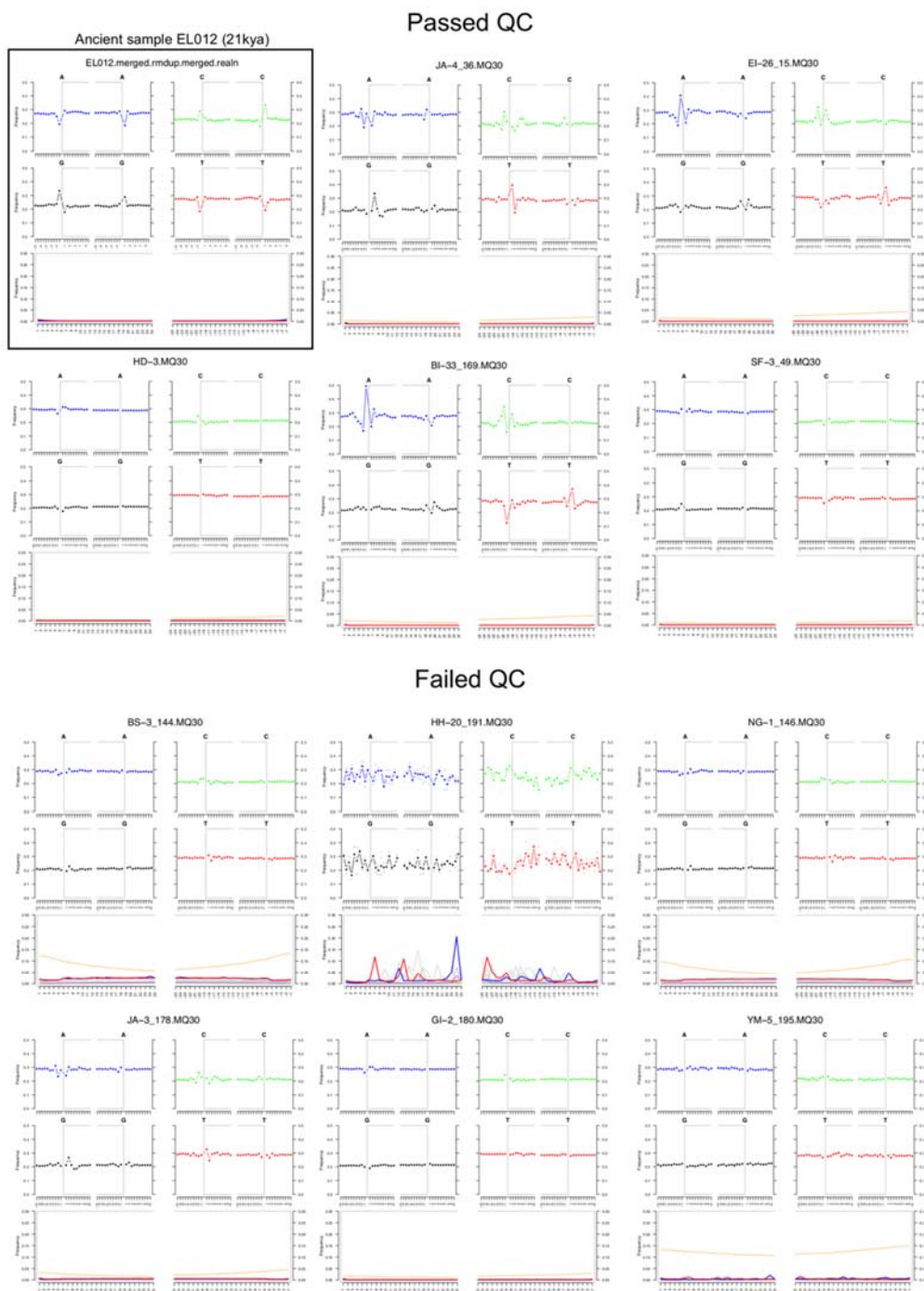
Figure S27. Deamination rates estimated from mapDamage in a subset of samples illustrating the range of patterns observed in the dataset. The one ancient sample included in the study is highlighted to show that thanks to the USER-treatment, it does not show an excess of damage compared to the modern samples.
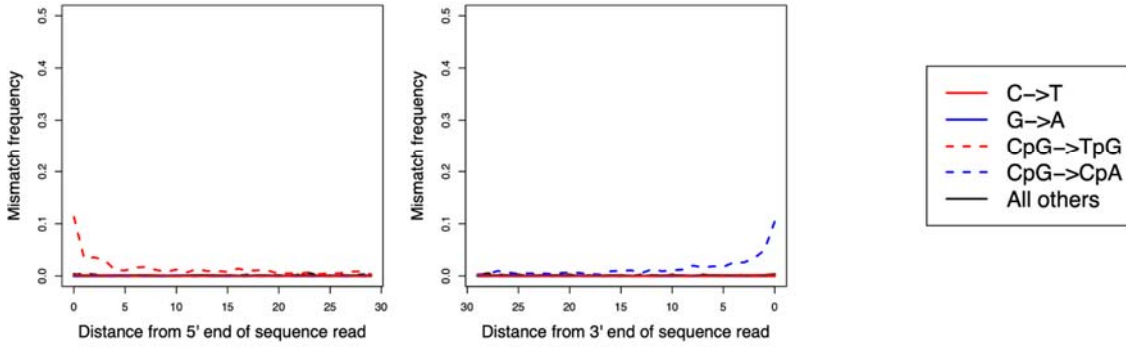
Figure S28. Deamination-derived damage patterns in the ancient Siberian sample estimated separately for CpG and non-CpG sites, showing that the USER-treatment removing ancient DNA damage worked efficiently in non-CpG sites. The elevated error rate observed in Figure S19 is, thus, likely driven by the CpG sites.
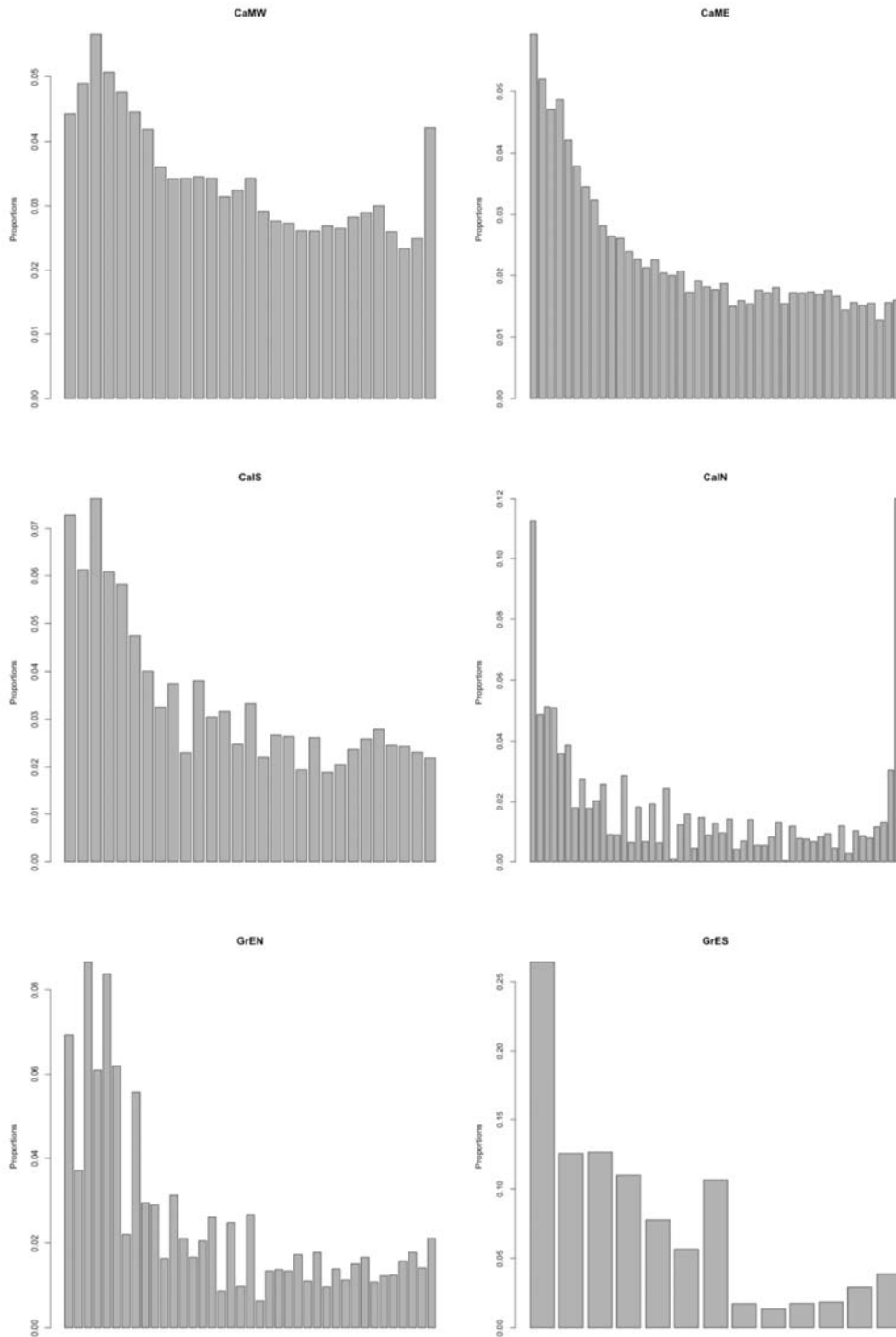
Figure S29. One-dimensional (1d) SFSs per population estimated by generating saf files in ANGSD using the -doSAF 1 option, the GATK model (-gl 2), filtering for mapping and base qualities (-minQ 30 -minMapQ 30) and using the filtered sites.
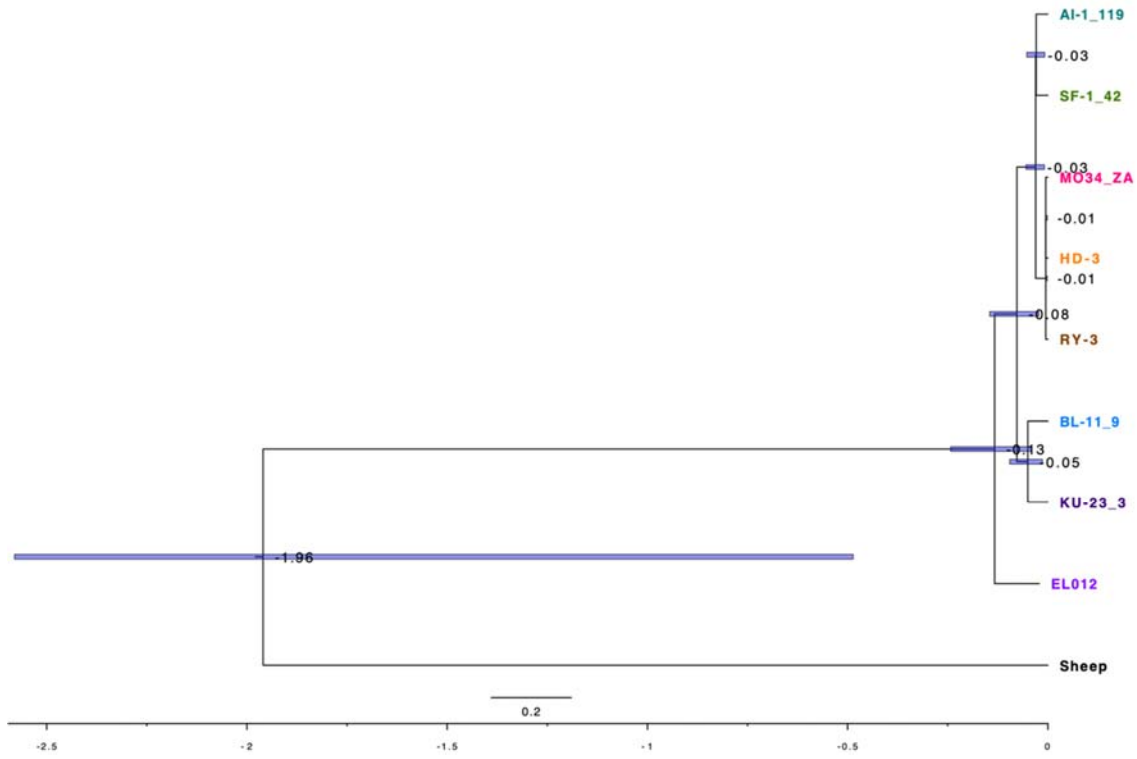
Figure S30. Nuclear dated phylogeny generated with IQTREE. Only the highest coverage sample from each region was used. The sheep was used as an outgroup.
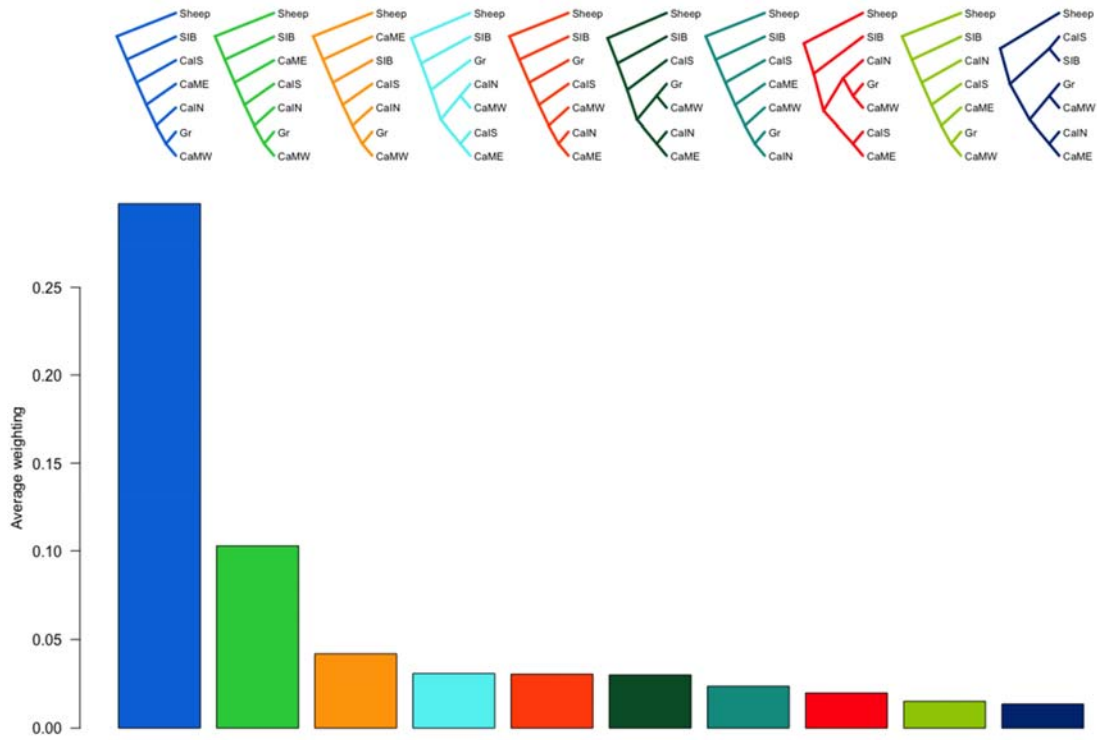
Figure S31. Weighing of topologies across 18 chromosomes of the sheep-mapped data estimated in Twisst.